PROCEEDINGS OF THE ROYAL SOCIETY A

Proc. R. Soc. A (2008) **464**, 595–612
doi:10.1098/rspa.2007.0161
Published online 18 December 2007

Ballistic dispersion in temperature gradient focusing

By David E. Huber* and Juan G. Santiago

Department of Mechanical Engineering, Stanford University, Stanford, CA 94305-3030, USA

Molecular dispersion is caused by both molecular diffusion and non-uniform bulk fluid motion. While the Taylor–Aris dispersion regime is the most familiar regime in microfluidic systems, an oft-overlooked regime is that of purely kinematic (or ballistic) dispersion. In most microfluidic systems, this dispersion regime is transient and quickly gives way to Taylor–Aris dispersion. In electrophoretic focusing methods such as temperature gradient focusing (TGF), however, the characteristic time scales for dispersion are fixed, and focused peaks may never reach the Taylor limit. In this situation, generalized Taylor dispersion analysis is not applicable. A heuristic model is developed here which accounts for both molecular diffusion and advective dispersion across all dispersion regimes, from pure diffusion to Taylor dispersion to pure advection. This model is compared to results from TGF experiments and accurately captures both the initial decrease and subsequent increase in peak widths as electric field strength increases. The results of this combined analytical and experimental study provide a useful tool for estimation of dispersion and optimization of TGF systems.

Keywords: microfluidics; temperature gradient focusing; kinematic dispersion; Taylor–Aris; ballistic; electroosmotic flow

1. Introduction

Dispersion, the natural tendency for ordered molecules to spread into disorder, is caused by both molecular diffusion and bulk fluid motion in the presence of shear (Taylor 1953). High dispersion rates may be advantageous for mixing and chemical reactions but are undesirable in separation and purification applications. For separations, minimizing dispersion improves resolution and sensitivity (Bharadwaj *et al.* 2002) and yields improved dynamics for concentration and purification applications (Bharadwaj & Santiago 2005), while for mixing applications, increased dispersion typically yields shorter mixing times (Nguyen & Huang 2005; Bottausch *et al.* 2007). As a consequence, the physical processes that lead to dispersion have been a subject of intense interest for at least a century (Albert 1910). In recent years, the development of the concept of the micro total analysis system (μTAS) or 'lab on a chip' (Manz *et al.* 1993; Auroux *et al.* 2002; Reyes *et al.* 2002; Vilkner *et al.* 2004;

* Author and address for correspondence: Sandia National Laboratories, Microfluidics Department, PO Box 969, MS 9292, Livermore, CA 94551-0969, USA (david.huber@stanfordalumni.org).

Received 6 August 2007
Accepted 20 November 2007

Dittrich *et al.* 2006) has led to the further exploration of dispersion within microchannels. We present an analysis of dispersion for focusing systems, in particular, microfluidic temperature gradient focusing. Temperature gradient focusing, hereafter 'TGF' (Ross & Locascio 2002), is an electrophoretic separation and focusing technique which has seen recent application to separations of chiral enantiomers (Balss *et al.* 2004), neutral and hydrophobic analytes (Kamande *et al.* 2007), and small molecules in the presence of adsorbing serum proteins (Munson *et al.* 2007).

In the field of microfluidics, researchers are most familiar with dispersion caused by molecular diffusion and Taylor dispersion (Taylor 1953). In 1953, Taylor demonstrated that, under certain conditions, the cross-sectional average of the unsteady, three-dimensional concentration field within a channel evolves as a one-dimensional convective diffusion equation. (Note that this seminal work is also the first detailed study of dispersion in microchannels, as Taylor performed his experiments in 500 μm diameter tubes.) Here, the advective dispersion in the axial direction is balanced by radial diffusion, causing peak variance to increase linearly in time, with the characteristic slope determined by an effective dispersion coefficient. Taylor further demonstrated that, theoretically, all solute plugs flowing within a channel ultimately reach this limit given enough time (Taylor 1953, 1954). Subsequently, Aris proved that the (now named) Taylor regime could be unified with the pure diffusive regime by using an effective dispersion coefficient that was the sum of the molecular diffusivity and the Taylor dispersion coefficient (Aris 1956). The effective dispersion concept has proved to be extremely useful and has been extended to other geometries (Dutta & Leighton 2002), generalized using alternative analyses (Brenner 1990; Stone & Brenner 1999), and extended to apply to electroosmotic flows (Griffiths & Nilson 1999), electrophoresis in nanochannels (Pennathur & Santiago 2005) and TGF (Huber & Santiago 2007).

While the Taylor–Aris regime is the most common regime in microfluidic systems, an oft-overlooked regime in microfluidics is that of pure convective or kinematic dispersion (also examined by Taylor 1953). Also known as ballistic dispersion (Ajdari *et al.* 2006), kinematic dispersion is that which occurs on a short time scale, such that no appreciable diffusion takes place and suspended solutes follow the 'ballistic' trajectories given by their local streamlines. This leads to significant curvature in the concentration field, as the 'topological' concentration lines are stretched by shear in the fluid velocity profile. In microfluidic systems, specifically the case of a solute plug injected into a microchannel, this regime is transient and quickly gives way to Taylor–Aris dispersion due to the small characteristic channel dimensions. In channels with non-circular cross sections, the largest cross-sectional dimension must be considered when estimating transition to Taylor dispersion, otherwise the time to reach the regime will be underestimated, as will be the dispersion rate (Chatwin & Sullivan 1982; Ajdari *et al.* 2006).

Dispersion in focusing systems such as TGF differs from traditional Taylor dispersion in that the relevant dispersion time scale is the focusing time scale, which does not increase with time. As a result, focused peaks can be 'trapped' within the ballistic dispersion regime. In a previous work, we developed generalized dispersion theory for TGF which yielded results applicable to the Taylor–Aris regime. Here, we introduce a heuristic model of dispersion for

focusing systems applicable to the full dispersion space. The paper is organized as follows: we briefly review TGF focusing theory and then develop our dispersion model. Lastly, we describe our experimental results and compare with the theoretical predictions.

2. Analysis

As described previously (Ross & Locascio 2002; Huber & Santiago 2007), TGF focuses charged species by balancing an axially varying electrophoretic flux with a counterflow, causing each specie to focus at the location where its net mass flux sums to zero (figure 1). The variation in electrophoretic velocity is accomplished through the use of a buffer with a temperature-dependent ionic strength induced by a temperature gradient applied along the axis of the microchannel. Following the convention of Ross & Locascio (2002), the buffer ionic strength is represented by the non-dimensional function $f(T)$, where T is the buffer temperature. The electrophoretic velocity is then $u_{\mathrm{eph}} = \nu_{0,\mathrm{eph}} E_0 f$, where $\nu_{0,\mathrm{eph}}$ is the analyte's electrophoretic mobility at a defined reference temperature and E_0 is the reference field strength (defined as the current flux, I/A, divided by the reference conductivity, σ_0). Note, in some cases an analyte's mobility may have an additional temperature dependence, which may also be used to induce focusing. For more details see Ross & Locascio (2002).

As in most microchannel systems, the Reynolds number is much less than unity and the Debye length is several orders of magnitude smaller than the characteristic dimensions of the channel. We neglect net charge in the bulk flow caused by the conductivity and permittivity gradients (Lin *et al.* 2004) because the dispersion associated with electric body forces is small compared with that caused by both the externally and internally generated pressure-driven flow (Bharadwaj & Santiago 2005). The flow is then given by Stokes' equation, $0 = -\nabla p + \mu \nabla^2 \boldsymbol{u}$ using a non-uniform Helmholtz–Smoluchowski slip boundary condition, $u_{\mathrm{eo}} = \varepsilon \zeta E/\mu$. As argued by Santiago (2001), the Helmholtz–Smoluchowski equation remains applicable as a local slip velocity in flows where all of the parameters may be non-uniform, e.g. where u_{eo} is the local electroosmotic flow velocity at the interface between the bulk and charge layer, ε is the local permittivity, ζ is the local zeta potential, E is the local axial electric field and μ is the local viscosity.

We model our focusing system using a convection–diffusion equation incorporating a conservative electrophoretic flux term. As qualitatively proposed by Ross & Locascio (2002), the system may be represented as a one-dimensional convective diffusion equation using an effective diffusivity. Huber & Santiago (2007) formally derived the equation by performing a cross-sectional area average on the full transport equation to yield

$$\frac{\partial \bar{c}}{\partial t} + \bar{u}_{\mathrm{bulk}} \cdot \frac{\partial \bar{c}}{\partial x} + \frac{\partial}{\partial x}(\bar{u}_{\mathrm{eph}} \bar{c}) - \frac{\partial}{\partial x}\left(\frac{\partial \bar{D}}{\partial x} \bar{c}\right) = \frac{\partial}{\partial x}\left(D_{\mathrm{eff}} \frac{\partial \bar{c}}{\partial x}\right), \tag{2.1}$$

where overbars represent a cross-section average; c is the concentration; u_{bulk} is the bulk fluid velocity (equal to the sum of electroosmosis plus pressure-driven flow); u_{eph} is the electrophoretic velocity; D is the molecular diffusivity; and D_{eff} is the

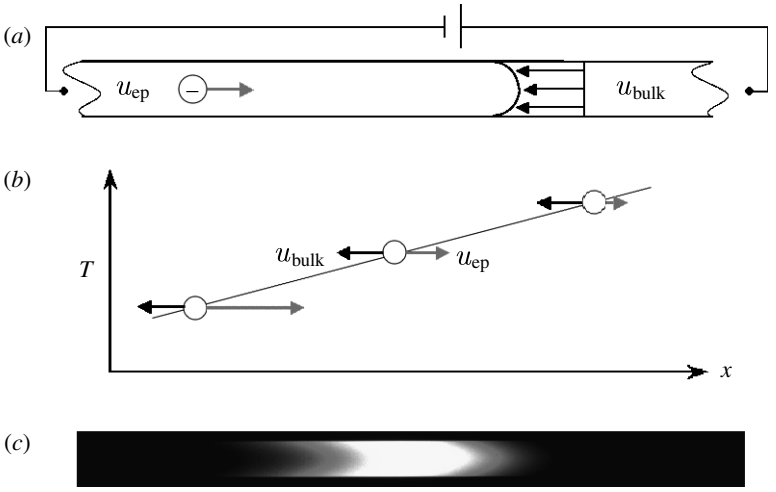

Figure 1. Schematic of TGF process with advective dispersion. (*a*) An electrophoretic velocity is countered by an opposing liquid flow, composed of both pressure-driven and electroosmotic flow. A temperature gradient is applied to a microchannel, inducing a gradient in the electrophoretic velocity of an analyte. (*b*) The analyte 'focuses' where the electrophoretic and convective fluxes sum to zero. Both molecular diffusion and advective dispersion broaden the band about the focus point. (*c*) Bodipy dye focused in a 20×200 μm wide channel with an applied electric field and temperature gradient of 60 V mm^{-1} and 10°C mm^{-1}, respectively.

effective dispersion coefficient that accounts for all off-axis transport effects. Note the diffusivity gradient term on the l.h.s., which represents a local drift velocity caused by an axial diffusivity gradient. It arises from the use of the Fokker–Planck diffusivity law, $\boldsymbol{J}=-\boldsymbol{\nabla}(Dc)$, for the diffusive flux in place of Fick's law, $\boldsymbol{\nabla}\cdot D\boldsymbol{\nabla}c$, which strictly applies only for homogeneous D (Van Milligen *et al.* 2005).

Interestingly, since equation (2.1) follows from an area-averaging procedure applied to the fully transient, three-dimensional, convective diffusion equation, it may be used to represent all dispersion regimes. The full decomposition also yields a deviation concentration equation in terms of c' (defined such that $c=\bar{c}+c'$), which determines the form of D_{eff}. To determine the dispersion regime, we define L as the characteristic length of an analyte peak, a as the channel half-width and U_{p} as the cross-section-averaged pressure-driven flow. The characteristic time scales are then L/U_{p} for axial advection and a^2/D for transverse diffusion. If the transverse diffusion time is much shorter than the advection time, we meet the Taylor–Aris scaling criterion (i.e. $L/a\gg U_{\mathrm{p}}a/D$).

In the Taylor–Aris regime, the deviation equation for convective diffusion reduces to a simple form where advective dispersion of the area-averaged concentration ($\bar{c}$) due to the deviation velocity (u') balances radial diffusion of deviation concentration, i.e. $u'\partial\bar{c}/\partial x\approx Dr^{-1}\partial(r\partial c'/\partial r)/\partial r$ (Taylor 1953; Stone & Brenner 1999). By solving for the deviation concentration in terms of the area-averaged concentration (Huber & Santiago 2007), we determine an analytical expression for D_{eff} as follows:

$$D_{\mathrm{eff}}=D+\kappa\frac{U_{\mathrm{p}}^2a^2}{D}\equiv D(1+\kappa Pe^2). \tag{2.2}$$

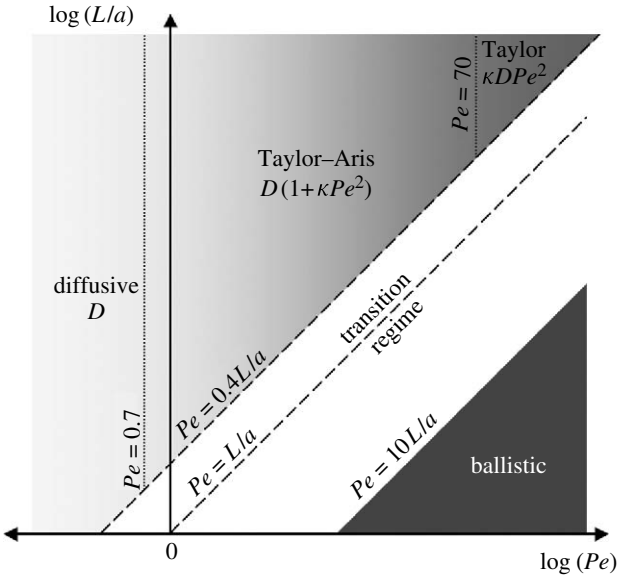

Figure 2. Dispersion regime map (modified from a similar plot in Probstein (1994)). The upper-left region contains the Taylor–Aris regime, with effective diffusivity $D(1+\kappa Pe^2)$, where κ is a constant determined by the channel geometry (e.g. 2/105 for parallel plates). This regime is subdivided into diffusive, Taylor–Aris and Taylor sub-regimes according to Taylor's scaling arguments (Taylor 1954). The lower-right region beneath the transition regime is the ballistic regime. L is the characteristic peak length, a is the characteristic channel half-width and L/a represents the non-dimensional diffusion time. Pe is $U_p a/D$, where U_p is the mean pressure-driven velocity, and D is the diffusivity at the focus point. For elution processes, L/a can be interpreted as a time axis. However, for focusing processes, L/a is a steady value set by electromigration and dispersion, which determine the characteristic dispersion regime.

Here, κ is a constant determined by the channel geometry (e.g. $\kappa = 2/105$ for parallel plates and 1/48 for a cylinder) and $Pe_a = U_p a/D$. Note that U_p is a local quantity and can vary axially due to internally generated pressure gradients (Herr *et al.* 2000). (Continuity is not violated because the total flow, i.e. pressure-driven plus electroosmotic, remains uniform.)

In regimes other than Taylor–Aris, the deviation equation becomes complex and includes gradients of the full three-dimensional concentration field. Consequently, we may no longer derive an explicit analytical expression for D_{eff}. Dispersion in these 'non-Taylor' regimes is the main subject of this paper. The current analysis is, to our knowledge, the first model of this 'ballistic' regime (Ajdari *et al.* 2006) for an electrophoretic focusing method.

Figure 2 summarizes the dispersion regime map as a function of L/a and Pe. Here, L can be interpreted as the characteristic length of the solute peak of interest (see below). The upper-left region contains the Taylor–Aris regime, beginning with purely diffusive dispersion at the left and transitioning towards Taylor dispersion at the right. Equation (2.2) above is applicable throughout this entire region, where the slope $(L/a)/Pe_a$ is larger than approximately 2.5 (Taylor 1954; Aris 1956). The lower-right region contains the transitional and ballistic regimes. For typical flow-through/elution processes, dispersion leads to continual

growth of the peak width. Thus the L/a axis may be considered a time axis. An initially sharp peak in the ballistic regime will grow in its width, ultimately satisfying $L/a \gg Pe_a$ and entering the Taylor–Aris regime. Until that point, D_{eff} is itself a function of time (Ajdari *et al.* 2006), and it is necessary to account for the additional dispersion incurred when passing through the ballistic and transitional regimes (Young & Jones 1991).

In contrast, for electrophoretic focusing processes, the characteristic length of the focused peak, L, maintains roughly the same value (after an initial focusing transient) even as the maximum concentration increases. This characteristic length is determined by the quasi-steady state balance between electromigration velocity gradients (providing focusing fluxes) and dispersion. Depending on the relative ratio of electromigration to dispersion fluxes, the axial dimension of the peak, L, may be larger than or on the order of the capillary radius a. For $L/a \gg Pe_a$, we can apply the Taylor–Aris approximation and equation (2.2) holds. However, for L/a of order Pe_a or less, the focused peak never attains the Taylor–Aris regime and remains fixed within either the ballistic or transitional regimes.

(*a*) *Dispersion model*

We wish to develop a model that provides a reasonable estimate for D_{eff} outside the Taylor–Aris regime. To do so, we first consider the hypothetical case of pure convective, or so-called 'ballistic' dispersion (Ajdari *et al.* 2006). This represents the limit where the focusing time scale is so short that species are unable to migrate across streamlines as they focus. Thus, each streamline will have an independent focal point. Once focused, molecules that migrate away from their respective focus locations in the spanwise, y, and transverse, z, directions via Brownian motion are 'instantly' focused to the new streamline's focal point. This represents a limit towards the opposite extreme of Taylor dispersion (where an individual molecule has sufficient time to sample all streamlines and thus focuses at the axial location, x, where the cross-sectional averaged velocities sum to zero). In the ballistic limit, instead of a single focus location, we now have a set of focus loci that are determined on a streamline-by-streamline basis as follows:

$$u_{\text{bulk}}(x,\, y, z) + u_{\text{eph}}(x,\, y, z) - \frac{\mathrm{d}D(x,\, y, z)}{\mathrm{d}x} = 0. \tag{2.3}$$

In principle, we can solve this equation for arbitrarily complex flow fields (e.g. those with varying internal pressure gradients, temperature gradients or geometries). In common practice, the velocity associated with the diffusivity gradient (the third term on the left) is several orders of magnitude smaller than the other velocity terms, so we neglect this term. For our analysis, we assume that spanwise temperature gradients are small, which makes the electrophoretic velocity solely a function of the axial dimension. We also assume that the change in electroosmotic slip velocity is small over the focus region. This allows us to treat the pressure-driven flow (internal plus external) as fully developed and independent of x. Doing so, we expand the bulk flow into its component parts and have

$$U_{\text{p}} + u'_{\text{p}}(y, z) + u_{\text{eo}} + E_0 \nu_0 f(T(x)) = 0, \tag{2.4}$$

where u'_{p} is the deviation pressure-driven velocity ($u'_{\mathrm{p}}(y,z) = u_{\mathrm{p}}(y,z) - U_{\mathrm{p}}$). If we redefine our axes so that the origin coincides with the cross-section averaged focal point, then $U_{\mathrm{p}} + u_{\mathrm{eo}} + E_0\nu_0 f(T(0)) = 0$. We may now solve for the focus position, x_{foci}, as a function of y and z. In particular, if we perform a Taylor series expansion of f about the focal point and use the first-order approximation, $f = f_1 x + f_0$, the resulting focus curve has a linear relationship between the deviation velocity, u'_{p}, and x_{foci}, as follows:

$$x_{\mathrm{foci}} = \frac{u'_{\mathrm{p}}(y,z)}{E_0\nu_0 f_1}, \tag{2.5}$$

where we include (y, z) as a reminder that u'_{p} depends on the cross-stream (i.e. spanwise and transverse) location.

Having derived a relation for the focus curve, we would like to determine its cross-sectional averaged dispersion. Unfortunately, the solution for our hypothetical case with purely ballistic dispersion yields a curve of zero width (for each streamline) and infinite local concentration. Physically, this pure ballistic limit is unrealizable. In practice, even with a very small focusing time scale, a balance will be reached between diffusive broadening and electrophoretic focusing. We instead offer here a more realistic approximation based on a heuristic argument for the balance of diffusion and electrophoresis. To this end, we consider replacing the concentration points (i.e. delta functions in concentration) by small concentration 'slices', whose concentration profiles are Gaussians in the x-direction. The size of the Gaussian is then given by the linearized one-dimensional focusing solution, which has the variance, $|D/E_0\nu_{\mathrm{eph},0} f_1| \equiv \alpha^2$ (Ross & Locascio 2002). This heuristic approach is motivated by our experimental observations that axial slices of focused peaks have profiles closely resembling Gaussians, even at significantly differing spanwise locations. We now solve for the variance, as follows:

$$\sigma^2 = \frac{\iiint x^2 c(x,\ y, z)\mathrm{d}x\,\mathrm{d}y\,\mathrm{d}z}{\iiint c(x,\ y, z)\mathrm{d}x\,\mathrm{d}y\,\mathrm{d}z}, \tag{2.6}$$

where

$$c(x,\ y, z) = c_0 \exp\left\{\frac{-(x - x_{\mathrm{foci}})^2}{2\alpha^2}\right\}.$$

Note that this definition of the variance assumes that the centre of mass for the concentration distribution is located at $x = 0$. This is appropriate given the linear relationship between the deviation velocity (which has zero mean) and focus location, provided that the mass distribution is approximately symmetric along any axial slice. Then,

$$\sigma^2 = \frac{1}{A_{\mathrm{c}}\alpha\sqrt{2\pi}} \iiint x^2 \exp\left\{\frac{-(x - x_{\mathrm{foci}})^2}{2\alpha^2}\right\}\mathrm{d}x\,\mathrm{d}y\,\mathrm{d}z, \tag{2.7}$$

where A_{c} is cross-sectional area of the channel. We may now perform the inner integration. Recognizing that this yields the second moment with respect to x, we write

$$\psi_x^2(y,z) = \frac{1}{\alpha\sqrt{2\pi}} \int x^2 \exp\left\{\frac{-(x - x_{\mathrm{foci}}(y,z))^2}{2\alpha^2}\right\}\mathrm{d}x. \tag{2.8}$$

Since the centre of mass, μ_x, is simply x_{foci} and the variance of each Gaussian is α^2, we use the relationship between the variance and the second moment to yield

$$\psi_x^2 = \sigma^2 + \mu_x^2 = \alpha^2 + (x_{\text{foci}})^2. \tag{2.9}$$

We can now solve for the variance of the full concentration distribution by performing the cross-sectional average

$$\sigma^2 = \alpha^2 + \left(\frac{U_{\text{p}}}{E_0 \nu_0 f_1}\right)^2 \cdot \overline{\hat{u}_{\text{p}}^2}, \tag{2.10}$$

where $\hat{u}_{\text{p}} = u'_{\text{p}}/U_{\text{p}}$, the mean-normalized deviation velocity. The variance of the full concentration distribution is thus the sum of the variance of the individual Gaussians plus the mean of the squared focus locations. Here we see that ballistic dispersion causes a surplus in variance above that given by the simple one-dimensional solution. The surplus variance is composed of two parts, the mean square of the normalized deviation, which is determined by the flow profile, and the specie's multiplier $U_{\text{p}}/E_0\nu_0 f_1$, which is a function of the specie, focus location and temperature gradient. Note that this multiplier is independent of electric field as U_{p} is directly proportional to E_0 provided the mean focus location and the channel temperature profile remain constant (i.e. when Joule heating is negligible). This variance thus represents the asymptotic limit for the case of pure convective dispersion.

(*b*) *Transitional dispersion*

As described earlier, the Taylor–Aris regime occurs when axial advective dispersion is balanced by radial diffusion. As we enter the transitional regime, diffusion gradually loses ground versus convective dispersion. Alternatively, from a Lagrangian perspective, the time scale for focusing is too short for solutes to sample all streamlines in an unbiased fashion, but too long to neglect the effect of diffusion entirely. We therefore modify our ballistic model to account for the fact that solutes now only sample nearby streamlines. We replace the deviation velocity of equation (2.10) with a weighted average of the local streamlines, u_{c}, to give

$$\sigma^2 = \alpha^2 + \left(\frac{U_{\text{p}}}{E_0 \nu_0 f_1}\right)^2 \cdot \overline{u_{\text{c}}^2}. \tag{2.11}$$

To determine u_{c}, we convolve $\hat{u}'_{\text{p}}$ with a symmetric Gaussian kernel which approximates the velocity averaging that occurs as solutes diffuse across streamlines. Consequently, the variance of this convolution kernel, $K(y,z)$, is proportional to the product of the diffusivity and the characteristic focus time, $\tau_{\text{foc}} = 1/2E_0\nu_0 f_1$, so the kernel takes the form

$$K(y,z) \sim \exp\left\{\frac{-y^2 - z^2}{4Dk\tau_{\text{foc}}}\right\} = \exp\left\{\frac{-y^2 - z^2}{4k\alpha^2}\right\}, \tag{2.12}$$

where k is a constant of proportionality. This heuristic kernel function is based upon the probability distribution for the location of a diffusive particle centred on the focal location of each streamline. This is an approximation to an ideal kernel, which must account for both the conditional probability of particles

starting on remote streamlines to jump to the designated streamline and the amount of time each particle samples the intervening streamlines. In general, nearby streamlines are disproportionately represented. Consequently, the constant, k, is less than unity and biases the kernel to weigh nearby streamlines preferentially. For sufficiently small focusing times, this heuristic solution recovers the pure ballistic dispersion result.

Lastly, in order to compare our transitional/ballistic results with the traditional Taylor–Aris results, we write (2.11) in terms of an effective diffusivity, using $\sigma = \sqrt{D_{\mathrm{eff}}/E_0 \nu_{\mathrm{eph},0} f_1}$, to get

$$D_{\mathrm{eff}} = D_{\mathrm{mol}} \left\{ 1 + Pe^2 \left(\frac{\alpha}{a}\right)^2 \overline{u_{\mathrm{c}}^2} \right\} = D_{\mathrm{mol}} \{1 + Pe^2 F(\alpha/a)\}, \tag{2.13}$$

since our convolved velocity profile and its variance, $\overline{u_{\mathrm{c}}^2}$, are also functions of α/a. We find that our heuristic theory leads to a result very similar to the Taylor–Aris dispersion coefficient, but with a Peclet number modified by the function, F, that accounts for both convective and geometric effects.

(*c*) *Two-dimensional Hybrid ballistic/Taylor dispersion*

For our experimental system, with its high aspect ratio rectangular cross-section, we generally find ourselves in the Taylor–Aris regime in the depth direction, but in the hybrid regime in the width direction. In this case, we may reduce the dimensionality of our model by one. To do so, we integrate out the z-dependency and replace the diffusivity with the Taylor–Aris dispersion coefficient within alpha in equation (2.11). Additionally, we replace v with its depth-averaged analogue by using the analytical series solution for Poiseuille flow in a rectangular channel (Doshi *et al.* 1978; White 1991), averaging the velocity in the depth direction and convolving with $K(y,z)$ as before. The result is an effective dispersion coefficient for the depth-averaged concentration field with the same form as equation (2.13), but with the molecular diffusivity everywhere replaced by the Taylor–Aris dispersion coefficient for the depthwise parallel plates solution.

3. Experimental set-up

We present here only a brief summary of the experimental set-up. A detailed description of the set-up used here is given by Huber (2006) and Huber & Santiago (2007). Our experiments were performed with Tris-borate-focusing buffer, composed of 900 mM Tris (hydroxymethyl)-aminomethane and 900 mM boric acid (Sigma Aldrich, St Louis, MO). For focusing experiments, we prepared solutions of the fluorescent dyes Bodipy propionic acid and Oregon Green 488 carboxylic acid (Invitrogen Corporation, Carlsbad, CA) using in-house deionized water which was filtered with a 0.2 μm filter (Nalgene, Rochester, NY) prior to use. For our microchannels, we used 50 mm long rectangular borosilicate glass capillaries (Vitrocom, Inc., Mountain Lakes, NJ) with nominal inner dimensions of 20×200 μm. The capillaries were mounted on a microscope slide and the slide was mounted across two thermally regulated copper blocks, maintained at different temperatures. The axial temperature gradient was induced where the capillary spanned a 2 mm gap between the blocks.

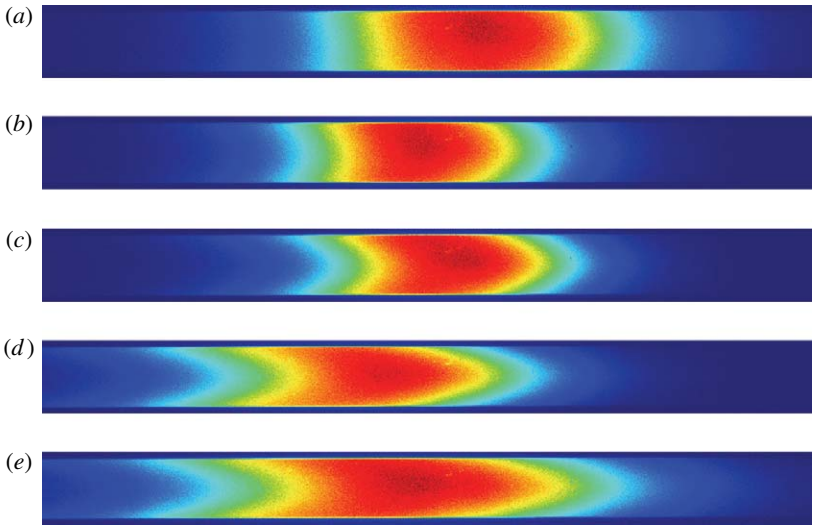

Figure 3. Full-field intensity images of focused Bodipy dye as a function of electric field strength. The images show the focusing of negatively charged Bodipy dye within a 23×230 μm rectangular capillary. The applied temperature gradient was 10°C mm^{-1} and the applied electric fields ranged from −10 to −80 V mm^{-1}, yielding current-normalized fields, E_0, of (*a*) −19, (*b*) −38, (*c*) −81, (*d*) −212 and (*e*) −345 V mm^{-1}. The net flow is right to left, driven by electroosmosis. The applied pressure head increases from 4 mm H_2O in (*a*) to 35 mm H_2O in (*e*), with the pressure-driven flow component supporting the rightward electrophoretic flux.

Huber & Santiago also give detailed descriptions of the control and calibration of this set-up including buffer conductivity, electroosmotic mobility and temperature field measurements. We simply note that at the high fields used in the focusing experiments presented here, Joule heating was significant and led to rises in absolute temperature within the channel. Within the gradient region, the axial temperature profile remained approximately linear, although the temperature difference across the gradient region decreased since Joule heating was a greater disturbance in the lower-temperature (more electrically resistive) liquid (Huber 2006). The change in temperature gradient with field was included in our subsequent dispersion calculations.

4. Temperature gradient focusing results

In our previous study (Huber & Santiago 2007), we performed a series of focusing experiments at low field and Peclet number, which captured the behaviour expected within the Taylor–Aris regime. In the present work, we performed experiments to examine wider TGF experiments with a variety of fluorescent analytes, under a range of applied electric fields, $\Delta V/L$, and nominal temperature gradients, $\Delta T/L$, and explored the system behaviour at high fields. Figure 3 shows sample full-field fluorescence images of focused Bodipy propionic acid with $\Delta T/L = 10$°C mm^{-1} and $\Delta V/L = 10$–100 V mm^{-1}. The applied head increases roughly linearly, with 4 mm H_2O applied for the 10 V mm^{-1} field and 35 mm H_2O for 80 V mm^{-1}. The direction of electrophoretic flux is left to right, while the bulk flow is right to left,

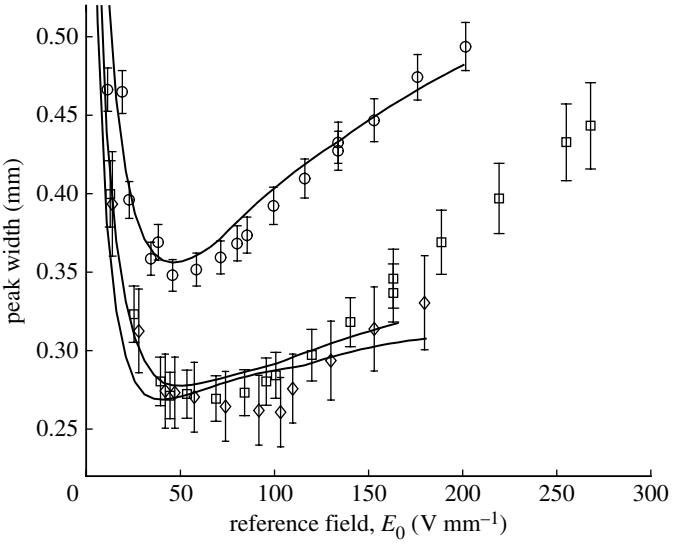

Figure 4. Bodipy peak width as function of reference field at three applied temperature gradients. Plotted are the standard deviations for the Gaussian fit to the intensity profile data. Error bars show the 95% CI of the peak width based on error propagation of the positional uncertainty. The solid lines show the theoretical width for each temperature gradient assuming focusing at the mean focus location with hybrid Taylor ballistic dispersion. For all series, $\nu_0 = -0.6\times10^{-8}\,\mathrm{m^2\,V^{-1}\,s^{-1}}$ and $D_0 = 5\times10^{-10}\,\mathrm{m^2\,s^{-1}}$. D, f_1 and U_p are determined from the focus location, temperature gradient and field as described in the text. U_p at the mean focus point was determined by a polynomial fit to the U_p versus E_0 data (see text). The theory lines were least-squares fits to the data, yielding the bias constant $k=0.03$ from equation (2.12) for all cases. Open circle, 20–40°C; open square, 20–60°C; open diamond, 20–80°C; solid line, theory.

driven predominantly by electroosmosis. The positive head supports the electrophoretic flux by slightly reducing the net bulk flow. The associated pressure gradient yields concentration fields similar to the pressure-driven flow of a neutral species (although here the peak is relatively stationary).

Additional focusing experiments (not shown) revealed the presence of multiple focusing peaks, suggesting the possibility that the Bodipy dye had reacted with the buffer to form multiple species, possibly through a reaction of the propionic acid with the primary amine of Tris (Huber & Santiago 2007). (Note, in general, we found that many of the dyes used had multiple focusing peaks. This may be a consequence of the fact that most commercially available dyes are reactive and intended for conjugation with proteins or other biological molecules.) The primary consequences for the present work is that the electrophoretic mobilities and diffusivities differ from those measured with borate buffer (for example Bharadwaj *et al.* 2002). For the experimental results presented in figures 3 and 4, focusing was performed upon a relatively slow (i.e. lower magnitude mobility) Bodipy peak in order to facilitate flow control.

The complete high-field results using the selected Bodipy peak are summarized in figure 4. In each series, the left-hand regulating block was set to 20°C, while the right-hand block was set to 40, 60 and 80°C. (The results for the 20/40°C case correspond to the images in figure 3.) The error bars show the 95% CI based upon an error propagation estimate of the standard deviation in focus position measured

for the full dataset. Qualitatively, figure 4 shows the expected trends. Peak widths decrease with increasing temperature gradients and, at low fields, decrease with increasing fields. As the field strength grows, advective dispersion (as witnessed by the increased curvature in figure 3) increases and peak widths grow.

To generate the predictions for the peak width shown in figure 4, we required independent estimates of all parameters in equation (2.11), in particular ν_0, D, U_p and f_1. Given the uncertainty in the composition of the peak specie, we first obtained independent estimates of the electrophoretic mobility and diffusivity. To this end, we used the net zero flux condition at the focus location, $u_\mathrm{eph}(\nu_\mathrm{eph,0}) + u_\mathrm{eo}(\nu_\mathrm{eo,0}) = -u_\mathrm{p}$, with a low-field subset of the focusing conditions (for which we had measurements of x_foc, u_p and temperature), and solved the over-determined model for the electrophoretic mobility using least-squares optimization. This yielded our estimate of $\nu_\mathrm{eph,0} = -0.6\times10^{-8}\,\mathrm{m^2\,V^{-1}s^{-1}}$, which agreed well with our previous results (Huber & Santiago 2007). To estimate diffusivity, we fit peak variance with $\sigma(t)^2 = \sigma_0^2 + 2Dt$ immediately following deactivation of the electric field, from which we measured D at each focus temperature. By taking the ratio of the Stokes–Einstein equation at T and $T_0 = 20$°C, we obtained the expression, $D(T)/D_0 = (T+273)\mu_0/293\mu(T)$, where μ_0 is the viscosity at T_0. We then extrapolated each diffusivity measurement to the reference temperature, yielding the mean reference value $D_0 = 5\times10^{-10}\,\mathrm{m^2\,s^{-1}}$.

For f_1, we assumed a uniform focus location equal to the mean position for the data series. The focus temperature and temperature gradient were then determined from the temperature profile. Multiplying the temperature gradient by $\mathrm{d}f/\mathrm{d}T$ at the focus temperature yielded the focusing parameter, f_1. In general, the magnitude of f_1 decreased with increasing field due to the growth in Joule heating. The heating simultaneously reduced the temperature gradient and raised the focus temperature, which also reduced the magnitude of $\mathrm{d}f/\mathrm{d}T$. (See Ross & Locascio (2002) for a plot of f versus T for 900 mM Tris-borate.) For the 20/40°C case, the range was -34 to $-22\,\mathrm{m^{-1}}$, while for 20/60 and 20/80°C the ranges were -63 to $-33\,\mathrm{m^{-1}}$ and -73 to $-29\,\mathrm{m^{-1}}$, respectively. Note that the f versus T curve flattens at higher temperature, so f_1 is not simply proportional to the difference between the end point temperatures.

To determine U_p, we used the same zero electric field data from which we generated the diffusivity estimate. Here we measured the location of the moving peak versus time. Since the variation around the mean focus location led to a variation in U_p, we fit the resulting U_p versus E_0 data with quadratic polynomials to smooth the variation and generate an estimate for U_p at the mean focus location. The resulting relations were $U_\mathrm{p}(E_0) = (-1.69\times10^{-15})E_0^2 + (1.32\times10^{-9})E_0 + 2.73\times10^{-6}$ for 20/40°C with $R^2 = 0.995$; $(2.49\times10^{-21})E_0^3 + (-3.23\times10^{-15})E_0^2 + (1.54\times10^{-9})E_0 - 3.03\times10^{-6}$ for 20/60°C with $R^2 = 0.997$; and $(-3.92\times10^{-15})E_0^2 + (2.01\times10^{-9})E_0 + 4.95\times10^{-6}$ for 20/80°C with $R^2 = 0.997$, where U_p is in $\mathrm{m\,s^{-1}}$ and E_0 is in $\mathrm{V\,m^{-1}}$. For the 20/40°C and 20/60°C cases, we fit data between 0 and 275 $\mathrm{V\,mm^{-1}}$. For the 20/80°C case, we fit data for fields between 0 and 180 $\mathrm{V\,mm^{-1}}$. In the latter case, the experimental results above 180 $\mathrm{V\,mm^{-1}}$ varied significantly. We attribute the irreproducibility to a number of factors stemming from the high amount of Joule heating. In particular, as the temperature elevates within the channel, air bubbles would frequently nucleate

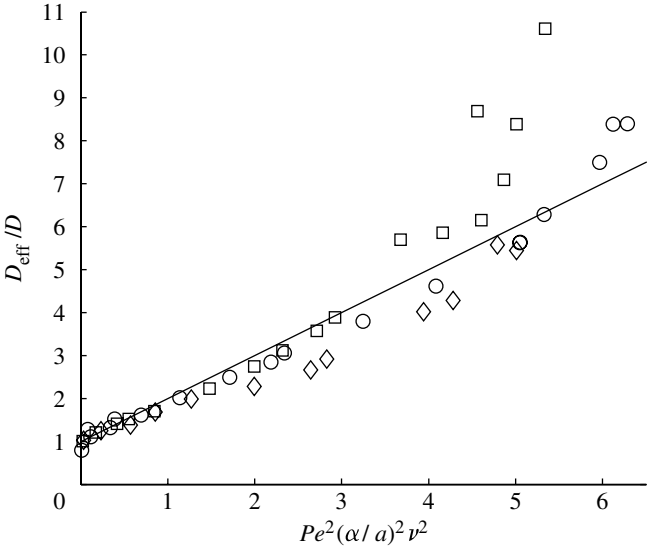

Figure 5. Effective dispersion ratio versus modified Peclet number for Bodipy at three temperature gradients. The data points collapse to the expected scaling (solid line, from equation (2.13)) with scatter observed at high *Pe*, where Joule heating effects are significant. For all data series, $\nu_0 = -0.6\times10^{-8}\ \mathrm{m^2\,V^{-1}s^{-1}}$ and $D_0 = 5\times10^{-10}\ \mathrm{m^2\,s^{-1}}$. U_{p} is determined on a pointwise basis (i.e. no polynomial fit), as are D_{foc} and f_1. From these, Peclet number, α and ν are calculated. Note the excellent match for the 20–40°C data. We attribute the greater scatter in the 20–60 and 20–80°C data both to their greater Joule heating and the temperature-influenced reaction of Bodipy propionic acid (as discussed in the text). Open circle, 20–40°C; open square, 20–60°C; open diamond, 20–80°C; solid line, predicted scaling.

and partially occlude the channel. Also, as noted by Huber & Santiago, propionic acid is reactive with the primary amine of Tris producing several species whose equilibrium concentration ratios are dependent on pH and temperature (Kemp & Vellaccio 1980). The consequent variation in electrophoretic mobility would also contribute to the irreproducibility.

We then performed a least-squares fit of the theoretical peak widths to the experimental data using k, from (2.12), as a single empirical fitting parameter. This yielded an excellent match with $k=0.03$ for the full 20/40°C data. This value was then used for the 20/60 and 20/80°C series. Figure 4 shows that the fits (using k as a single fitting parameter) to the experimental data are fairly good. The semi-empirical model captures the Taylor–Aris regime very well (as expected), and the transition between Taylor dispersion- and ballistic dispersion-dominated regimes. We present model predictions for the 20/60 and 20/80°C cases up to a maximum field of 165 and 180 $\mathrm{V\,mm^{-1}}$, respectively. At such fields, Joule heating is significant, resulting in highly non-uniform temperature fields, and the model assumptions clearly break down.

For figure 5, we determine the experimentally observed dispersion coefficient, $D_{\mathrm{eff,meas}}$, by dividing measured peak width by $E_0\nu_0 f_1$. The figure shows a scaling of the dispersion coefficient by diffusivity versus the modified Peclet number of (2.13). The data collapse well up to approximately $Pe^2(\alpha/a)^2v^2=3$. At higher values (corresponding to the highest fields), there is a trend towards greater

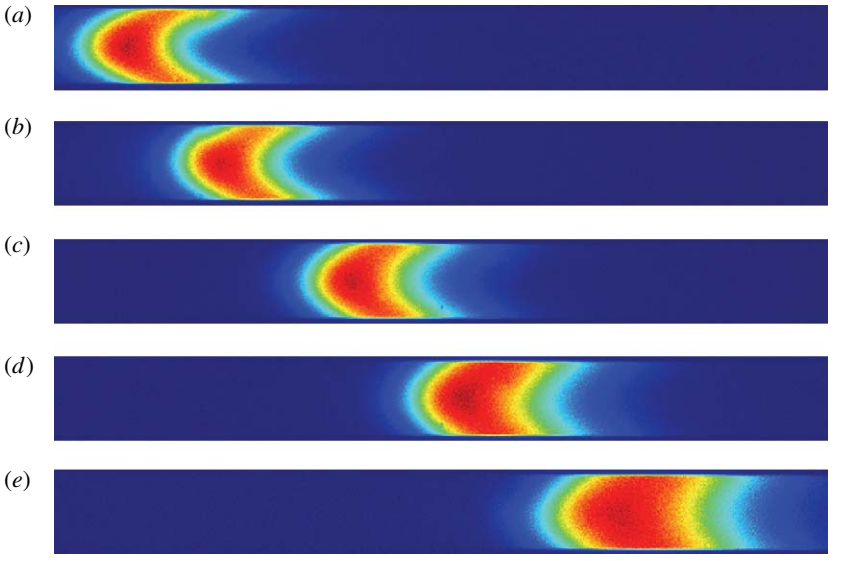

Figure 6. (*a–e*) TGF scanning images of Oregon Green dye. The images show a focused band of negatively charged Oregon Green carboxylic acid scanned through the gap region by a gradual increase of the pressure head. The applied temperature gradient was 35°C mm^{-1} and the applied electric field was $-40\ \mathrm{V\ mm}^{-1}$. From top to bottom, images were captured at relative times of 0, 60, 90, 120 and 150 s.

dispersion values. This is consistent with the breakdown of the uniform temperature gradient assumption as high amounts of Joule heating begin to induce both axial and spanwise temperature non-uniformities. We also observe significant scatter in the 20–60 and 20–80°C cases, which we attribute to changes in the specie's electrophoretic mobility (as described above).

(*a*) *Dispersion optimization*

Figure 4 highlights the trade-off between increased focusing strength and field-dependent dispersion as electric field is raised. In TGF, high electric fields can cause advective dispersion. In any TGF device where advective dispersion is significant, there will then be an optimum range of field strengths that minimizes peak width at a given temperature difference. Further, since both dispersion and the focusing parameter, f_1, are strong functions of absolute temperature, peak width has a spatial dependence (through the focus temperature), even for fixed electric field and temperature gradient. Here we demonstrate this spatial dependence of $D_{\mathrm{eff,meas}}$ with data obtained during a scanning TGF experiment (Hoebel *et al.* 2006). In this experiment, we focused Oregon Green carboxylic acid while slowly increasing the applied pressure difference, causing the pseudo-steady peak to traverse (or 'scan') through the temperature gradient region. For this experiment, the cold and hot blocks were set to 10 and 80°C, and the applied field was $40\ \mathrm{V\ mm}^{-1}$, which corresponded roughly with the optimum field strengths suggested by figure 4. As with Bodipy, the scanning experiment revealed two primary peaks and multiple weaker peaks. Figure 6 shows images of the faster of the primary peaks, as it progresses through the gap region. When the peak is in the colder, left-hand region, diffusivity is reduced and the advective dispersion is stronger, as indicated by the

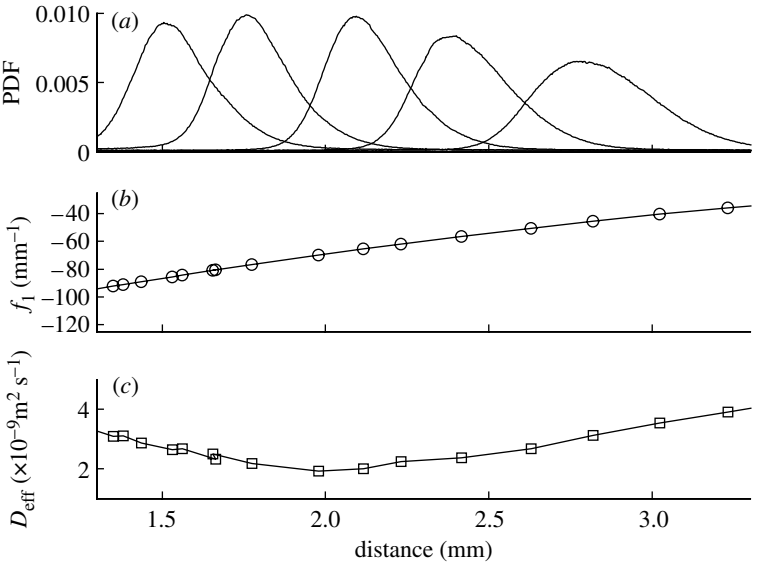

Figure 7. Scanning profiles of Oregon Green with axial dispersion dependence. (*a*) Width-averaged axial intensity probability density functions (PDF) for the Oregon Green bands shown in figure 6. (*b*) Focusing parameter, f_1, at all scanned locations as determined from f versus T and temperature field measurements. (*c*) Calculated effective dispersion coefficient based on the electrophoretic mobility of Oregon Green ($\nu_0 = -5\times10^{-8}$). The applied temperature gradient was 35°C mm^{-1} and the applied electric field was constant at -40 V mm^{-1}.

high degree of curvature in the spanwise direction. As it enters the hot region, diffusive fluxes increase and the curvature associated with advective dispersion is less apparent.

In figure 7, we normalize the axial profiles shown in figure 6 to yield the intensity probability distribution functions (PDFs) for the five peaks. Plotted with the PDFs are the focusing parameter, f_1, calculated from the temperature profile, and the effective dispersion, determined by assuming an electrophoretic mobility for Oregon Green of $\nu_0 = -5\times10^{-8}$ m^2 V^{-1}s^{-1}. The dispersion decreases initially before beginning its expected climb with increasing temperature along the gap. While this suggests that the advective dispersion is being reduced by an amount greater than the increase in molecular diffusivity, since the scanning was performed left to right, it is also possible that the leftmost peaks were still decreasing in width, having not yet reached the pseudo-steady profile. In order to determine the behaviour of the advective dispersion velocity scale, U_{p}, measurements of this quantity would be required at each location, something that was not possible with this experiment. In any case, it is clear that there exist both optimal field values and optimal focusing locations for TGF experiments.

5. Conclusion

In this work, we have extended our generalized dispersion model (Huber & Santiago 2007) across the full range of dispersion regimes (i.e. pure diffusion through Taylor–Aris and ballistic regimes). We have shown that the application

of a cross section-averaged, one-dimensional, convective diffusion model is useful even at high Peclet numbers (and correspondingly high electric fields), provided the effective dispersion coefficient is modified to include ballistic dispersion effects.

The various dispersion regimes have different consequences for the focusing performance of TGF. At sufficiently low fields (with their correspondingly low pressure-driven flow velocities), the steady-state focused peak width decreases with increasing field, and molecular diffusivity is the primary source of dispersion. At higher fields, the system may enter the Taylor–Aris dispersion regime ($Pe_w \ll L/w$). Here dispersion may be represented by a traditional Taylor–Aris dispersion coefficient. At higher fields, or in situations where $Pe_w \ll L/w$ is violated, the dispersion becomes ballistic in form and steady-state peak widths increase sharply with applied field. Ballistic dispersion in TGF occurs when molecules disperse along streamlines of the non-uniform bulk flow because the time scale for focusing is smaller than the time for a molecule to diffuse across the channel cross-section. The regime is indicated by an observable induced curvature in the concentration field. For high fields, the dispersion coefficient must account for these ballistic dispersion effects. Our heuristic theory yields a dispersion coefficient that accurately models focused peak widths in this regime. Lastly, we note that at even higher field strengths (depending on the system geometry and heat transfer characteristics), Joule heating leads to spanwise temperature gradients, which introduces additional electrophoretic and diffusional dispersive forces. At such extreme fields, our depth-averaged formulation and dispersion arguments fail, and it becomes necessary to model the coupled three-dimensional temperature, concentration and velocity fields in order to accurately determine the dispersion.

Despite these complexities, our results show that TGF performance is readily optimized empirically, even when a detailed understanding of the heat transfer and its associated dispersion components is unavailable. Both optimal field strengths (as suggested by figure 4) and best focusing locations (see figure 7) may be determined for a given microchannel geometry and set of focusing conditions. System designers are advised to consider both optimal field strengths and minimum-dispersion focus locations when developing focusing systems.

This work was sponsored by the National Institutes of Health (grant N01-HV-28183) and a NSF PECASE Award (J.G.S., award number NSF CTS0239080) with Dr Michael W. Plesniak as award monitor. D.E.H. was supported by a NDSEG fellowship and ARCS scholarship.

References

Ajdari, A., Bontoux, N. & Stone, H. A. 2006 Hydrodynamic dispersion in shallow microchannels: the effect of cross-sectional shape. *Anal. Chem.* **78**, 387–392. (doi:10.1021/ac0508651)

Albert, G. 1910 On the movement of a coloured index along a capillary tube, and its application to the measurement of the circulation of water in a closed circuit. *Proc. Phys. Soc. Lond.* **23**, 190. (doi:10.1088/1478-7814/23/1/316)

Aris, R. 1956 On the dispersion of a solute in a fluid flowing through a tube. *Proc. R. Soc. A* **235**, 67–77. (doi:10.1098/rspa.1956.0065)

Auroux, P. A., Iossifidis, D., Reyes, D. R. & Manz, A. 2002 Micro total analysis systems. 2. Analytical standard operations and applications. *Anal. Chem.* **74**, 2637–2652. (doi:10.1021/ac020239t)

Balss, K. M., Vreeland, W. N., Phinney, K. W. & Ross, D. 2004 Simultaneous concentration and separation of enantiomers with chiral temperature gradient focusing. *Anal. Chem.* **76**, 7243–7249. (doi:10.1021/ac049046r)

Bharadwaj, R. & Santiago, J. G. 2005 Dynamics of field-amplified sample stacking. *J. Fluid Mech.* **543**, 57–92. (doi:10.1017/S0022112005005975)

Bharadwaj, R., Santiago, J. G. & Mohammadi, B. 2002 Design and optimization of on-chip capillary electrophoresis. *Electrophoresis* **23**, 2729–2744. (doi:10.1002/1522-2683(200208)23:16<2729::AID-ELPS2729>3.0.CO;2-I)

Bottauschi, F., Cardonne, C., Meinhart, C. & Mezic, I. 2007 An ultrashort mixing length micromixer; the shear superposition micromixer. *Lab Chip* **7**, 396–398. (doi:10.1039/b616104a)

Brenner, H. 1990 Macrotransport processes. *Langmuir* **6**, 1715–1724. (doi:10.1021/la00102a001)

Chatwin, P. C. & Sullivan, P. J. 1982 The effect of aspect ratio on longitudinal diffusivity in rectangular channels. *J. Fluid Mech.* **120**, 347–358. (doi:10.1017/S0022112082002791)

Dittrich, P. S., Tachikawa, K. & Manz, A. 2006 Micro total analysis systems. Latest advancements and trends. *Anal. Chem.* **78**, 3887–3908. (doi:10.1021/ac0605602)

Doshi, M. R., Daiya, P. M. & Gill, W. N. 1978 Three dimensional laminar dispersion in open and closed rectangular conduits. *Chem. Eng. Sci.* **33**, 795–804. (doi:10.1016/0009-2509(78)85168-9)

Dutta, D. & Leighton, D. T. 2002 A low dispersion geometry for microchip separation devices. *Anal. Chem.* **74**, 1007–1016. (doi:10.1021/ac010718c)

Griffiths, S. K. & Nilson, R. H. 1999 Hydrodynamic dispersion of a neutral nonreacting solute in electroosmotic flow. *Anal. Chem.* **71**, 5522–5529. (doi:10.1021/ac990714w)

Herr, A. E., Molho, J. I., Santiago, J. G., Mungal, M. G., Kenny, T. W. & Garguilo, M. G. 2000 Electroosmotic capillary flow with nonuniform zeta potential. *Anal. Chem.* **72**, 1053–1057. (doi:10.1021/ac990489i)

Hoebel, S. J., Balss, K. M., Jones, B. J., Malliaris, C. D., Munson, M. S., Vreeland, W. N. & Ross, D. 2006 Scanning temperature gradient focusing. *Anal. Chem.* **78**, 7186–7190. (doi:10.1021/ac060934r)

Huber, D. E. 2006 *Transport and dispersion in microfluidic temperature gradient focusing.* Stanford, CA: Stanford University.

Huber, D. E. & Santiago, J. G. 2007 Taylor–Aris dispersion in temperature gradient focusing. *Electrophoresis* **28**, 2333–2344. (doi:10.1002/elps.200600830)

Kamande, M. W., Ross, D., Locascio, L. E., Lowry, M. & Warner, I. M. 2007 Simultaneous concentration and separation of coumarins using a molecular micelle in micellar affinity gradient focusing. *Anal. Chem.* **79**, 1791–1796. (doi:10.1021/ac0617619)

Kemp, D. S. & Vellaccio, F. 1980 *Organic chemistry.* New York, NY: Worth Publishers.

Lin, H., Storey, B. D., Oddy, M. H., Chen, C.-H. & Santiago, J. G. 2004 Instability of electrokinetic microchannel flows with conductivity gradients. *Phys. Fluids* **16**, 1922–1935. (doi:10.1063/1.1710898)

Manz, A., Harrison, D. J., Verpoorte, E. & Widmer, H. M. 1993 Planar chips technology for miniaturization of separation systems: a developing perspective in chemical monitoring. *Adv. Chromatogr.* **33**, 1–6.

Munson, M. S., Meacham, J. M., Locascio, L. E. & Ross, D. 2007 Counterflow rejection of adsorbing proteins for characterization of biomolecular interactions by temperature gradient focusing. *Anal. Chem.* **80**, 172–178. (doi:10.1021/ac701900m)

Nguyen, N. T. & Huang, X. 2005 Mixing in microchannels based on hydrodynamic focusing and time-interleaved segmentation: modeling and experiment. *Lab Chip* **5**, 1320–1326. (doi:10.1039/b507548c)

Pennathur, S. & Santiago, J. G. 2005 Electrokinetic transport in nanochannels. 1. Theory. *Anal. Chem.* **77**, 6772–6781. (doi:10.1021/ac050835y)

Probstein, R. F. 1994 *Physicochemical hydrodynamics: an introduction.* New York, NY: Wiley.

Reyes, D. R., Iossifidis, D., Auroux, P. A. & Manz, A. 2002 Micro total analysis systems. 1. Introduction, theory, and technology. *Anal. Chem.* **74**, 2623–2636. (doi:10.1021/ac0202435)

Ross, D. & Locascio, L. E. 2002 Microfluidic temperature gradient focusing. *Anal. Chem.* **74**, 2556–2564. (doi:10.1021/ac025528w)

Santiago, J. 2001 Electroosmotic flows in microchannels with finite inertial and pressure forces. *Anal. Chem.* **73**, 2353–2365. (doi:10.1021/ac0101398)

Stone, H. A. & Brenner, H. 1999 Dispersion in flows with streamwise variations of mean velocity: radial flow. *Ind. Eng. Chem. Res.* **38**, 851–854. (doi:10.1021/ie980355f)

Taylor, G. 1953 Dispersion of soluble matter in solvent flowing slowly through a tube. *Proc. R. Soc. A* **219**, 186–203. (doi:10.1098/rspa.1953.0139)

Taylor, G. 1954 Conditions under which dispersion of a solute in a stream of solvent can be used to measure molecular diffusion. *Proc. R. Soc. A* **225**, 473–477. (doi:10.1098/rspa.1954.0216)

Van Milligen, B. Ph., Bons, P. D., Carreras, B. A. & Sanchez, R. 2005 On the applicability of Fick's law to diffusion in inhomogeneous systems. *Eur. J. Phys.* **26**, 913–925. (doi:10.1088/0143-0807/26/5/023)

Vilkner, T., Janasek, D. & Manz, A. 2004 Micro total analysis systems. Recent developments. *Anal. Chem.* **76**, 3373–3385. (doi:10.1021/ac040063q)

White, F. M. 1991 *Viscous fluid flow*. McGraw-Hill series in mechanical engineering. New York, NY: McGraw-Hill, Inc.

Young, W. R. & Jones, S. 1991 Shear dispersion. *Phys. Fluids A (Fluid Dyn.)* **3**, 1087–1101. (doi:10.1063/1.858090)